Thermal Disorder and Bond Anharmonicity in Cesium Lead Iodide Studied by Neutron Total Scattering and the Reverse Monte Carlo Method

Jiaxun Liu,[†] Anthony E Phillips,[*,†] David A Keen,[‡] and Martin T Dove[*,¶,†]

†*Centre for Condensed Matter and Materials Physics, School of Physics and Astronomy, Queen Mary University of London, Mile End Road, London, E1 4NS, UK*

‡*ISIS Facility, Rutherford Appleton Laboratory, Harwell Campus, Didcot, Oxfordshire, OX11 0QX, UK*

¶*Department of Physics, Sichuan University, No 24 South Section 1, Yihuan Road, Chengdu, People's Republic of China 610065*

E-mail: a.e.phillips@qmul.ac.uk; martin.dove@qmul.ac.uk

Abstract

Cesium lead iodide, $CsPbI_3$, combines promising optoelectronic applications with long-term chemical stability. It has a cubic perovskite crystal structure at temperatures above 600 K. Previous experimental work showed that the I atoms move substantially in directions perpendicular to the Pb – I – Pb linkages, while computational modelling shows that there are soft, anharmonic distortion modes for wave vectors at both the Brillouin zone centre and zone boundary. However, there has been no direct experimental probe of the energy profile associated with these distortions. We report here total neutron scattering data from a powder sample of this material as a function of temperature. We use reverse Monte Carlo modelling to construct

configurations of atoms consistent with both the local and long-range structure. Our key finding is that the Pb – I bonds are extremely anharmonic, and thus it follows that all near-neighbour bond distributions are significantly asymmetric. The distribution of nearest-neighbour Pb – I distances, with a long tail to distances up to around 120% of the distance corresponding to the peak in the distribution function, can be described as reflecting an underlying anharmonic bond potential energy function which is well-represented by the standard Morse potential with reasonable parameters.

Introduction

In recent years, hybrid organic-inorganic lead halide perovskites have received significant attention for potential applications in photovoltaic devices, due to the high efficiency, low cost and easy fabrication of this family of materials. The power conversion efficiency of solar cells based on the related material methylammonium lead iodide, $(CH_3NH_3)PbI_3$, initially reached 3.8% in 2009[1] but has recently passed 23.7%.[2] However, problems with long-term chemical stability and durability remain to be solved. For example, $MAPbI_3$ decomposes to CH_3I, NH_3 and PbI_2 when the temperature exceeds 80 °C for 20 minutes.[3] Since this instability is associated with the organic component, a promising alternative is provided by the closely related inorganic perovskites.[4]

One such material is $CsPbI_3$. Its band gap of $E_g = 1.73$ eV is suitable for photovoltaic applications, especially when the material is prepared in the form of quantum dots.[5] $CsPbI_3$ has two stable crystallographic phases at ambient pressure: the high-temperature cubic α phase with the ideal perovskite structure of cubic symmetry, space group $Pm\bar{3}m$ (Fig. 1a), and the low-temperature orthorhombic δ phase of space group *Pnma* (Fig. 1b). The two phases do not have a group-subgroup relationship: the cubic perovskite phase consists of corner-sharing PbI_6 octahedra, but in the orthorhombic phase these octahedra are edge-sharing. Moreover, the coordination number of cesium with respect to the iodine neighbors changes from 12 to 9 between the α and δ phases. The two phases transform to each other by a reversible first-order transformation with a wide co-existence temperature range around 40 K(560–600 K).[6] This phase transition has recently been exploited to

create thermochromic photovoltaic windows with excellent stability.[7] Undercooling the α phase below this transition results in the formation of metastable β (tetragonal, space group $P4/mbm$) and γ (orthorhombic, space group *Pbnm*) perovskite phases, both of which transform back to the thermodynamically-favoured δ phase over time.[8]

The first crystallographic study of the phase transition in $CsPbI_3$, performed using Rietveld refinement of synchrotron x-ray diffraction, reported anisotropic thermal motion of the iodine atoms, with significant motion transverse to the linear Pb–I–Pb linkages, in common with many other perovskites;[6] these results are consistent with neutron diffraction work on related materials such as $CsPbCl_3$.[9,10] However, as these latter authors point out, conventional diffraction methods cannot in principle distinguish whether (1) this is due to the growth of small clusters of lower symmetry than the parent cubic phase, as precursors of a phase transition, or (2) this reflects bond anharmonicity, in the sense that the distribution of atomic positions is not well described by a Gaussian.

One way of tackling this problem is by probing the atomic *dynamics* directly. Experimentally, this can for instance be done using inelastic neutron scattering measurements. In the closely related material $CsPbCl_3$, these confirm that the transverse acoustic modes remain below about 2 meV throughout the Brillouin zone, with low-frequency optic modes too at some special positions.[11] Computationally, one approach is to model the energy profile associated with normal modes. Density-functional perturbation theory calculations have revealed double-well potentials at both the Brillouin zone centre[12] and zone boundary.[13]

An alternative is to use scattering methods sensitive to the atomic *structure*. Although in principle this is distinct from the dynamics, such methods can nonetheless contribute to the problem in three ways. First, considering only the sharp Bragg diffraction peaks, high-resolution data can be used to refine multipole or split-site models. This approach was used in many early studies on $CsPbCl_3$, using both single-crystal[9,10] and powder samples,[14] although these were inconclusive as to whether transverse Cl motion had a double-well potential.[15] Second, the diffuse scattering, which corresponds to local deviations from the crystallographic average structure, can also be measured and the total scattering used to calculate the pair distribution function (PDF). Using "small-box"

refinement methods, this can be compared against known distorted structures, for instance those of the β or γ phases, to detect regions of lower local symmetry. This approach has been used to demonstrate that the cubic aristotype structure is inadequate to describe the local structure of $MAPbI_3$ and formamidinium lead iodide, although it was unclear whether this was best described by off-centring of the Pb ions, rotation of the PbI_6 octahedra, or both.[16]

We report here measurements using a third approach. We again take diffuse as well as Bragg scattering into account, but instead refine the positions of a "big box" of atoms against the PDF, the total scattering function, and the Bragg diffraction pattern, using the reverse Monte Carlo (RMC) algorithm.[17] This analysis produces atomic configurations that are consistent with all the experimental data, without reference to or bias towards any particular local distortion. These configurations therefore capture both the average structure as described by the distribution of atomic positions (the average structure and single-atom fluctuations) and the local structure that describes correlated atomic fluctuations, such as rotations of the PbI_6 octahedra. The "snapshot" configurations this method produces involve the superposition of many different distortion modes, with varying amplitudes, and thus complement rather than being directly comparable with inelastic or computational results concerning a single mode. Nonetheless, we show that particular features in the local structure can be associated with zone-centre or zone-boundary modes.

Experimental

The $CsPbI_3$ powder sample was synthesised from solution by literature methods.[18] Neutron scattering measurements were performed using the GEM diffractometer at ISIS. Short runs for crystal structure analysis were collected on heating in steps of 10 K from 543–673 K to observe the transition between the δ and α phases, and long runs suitable for total scattering analysis were collected at temperatures of 673, 643, 613 and 573 K with the sample remaining in the α phase on cooling, and total scattering data collection at 473 K and 293 K in the δ phase.

The raw data were transformed into diffraction patterns using the Mantid software.[19] Rietveld

refinement was performed using the EXPGUI interface to GSAS.[20,21] Total scattering functions were extracted from the raw data and background correction runs using the Gudrun software,[22] which was also used to calculate the PDF by Fourier transform of the total scattering function (see the ESI for more details and equations). RMC refinement was performed with the RMCprofile code, version 6.7.[17] Full details are given in the ESI; here we note that the RMC data sets contained the total scattering function $i(Q)$, pair distribution function $D(r)$ (both defined in the ESI) and the Bragg scattering profile.

Thirty independent RMC configurations were simulated from each data set in order to give good statistics in the subsequent analysis. Examples of the quality of agreement between the experimental data and the corresponding functions calculated by the RMC method are given in the ESI (Fig. S2).

Results and discussion

Crystal structure analysis

The results for Rietveld refinements (lattice parameters, atomic fractional coordinates, and atomic displacement parameters) for both α and δ phases are given in the ESI, Tables S1–S3.

The lattice parameters are shown as a function of temperature in scaled form (to allow for comparison of temperature dependence) in Figure 2. The three orthorhombic lattice parameters show similar thermal expansivity, with an average coefficient of linear thermal expansivity of 21 ± 1 MK^{-1}. The cubic phase shows positive thermal expansion with linear expansivity 52 ± 1 MK^{-1}, which is surprisingly around 2.5 times larger than for the orthorhombic phase, and we do not have a natural explanation for it yet.

The average structure of the α phase calculated from the RMC configurations agreed well with Rietveld refinement both in atomic positions and, more significantly, in the atomic displacement parameters. All atoms are on special positions with coordinates set by symmetry, and the average positions are consistent with the special positions to within 0.001 in terms of fractional coordinate. The ADPs calculated from the RMC configurations are given the ESI, Table S4. The ADPs from

RMC analysis were consistently slightly larger than from Rietveld refinement, which we attribute to the effects of attenuation of the neutron beam by the sample. We earlier noted that the ADPs for the iodine atom show much larger displacements in the two directions perpendicular to the Pb–I–Pb linear linkage than in the direction along the linkage, with the transverse mean-squared displacements being around 6 times larger than for the longitudinal mean-squared displacements. Actually, an even larger difference between the transverse and longitudinal mean-square displacements was obtained in the previous crystal structure analysis of reference 6,the difference is probably because the longitudinal mean-squared displacements are underestimated by a constant amount in that study, due to the effects of beam absorption. The ADPs of Cs and Pb are isotropic by symmetry in the Rietveld refinement, with the value for Cs being about twice as large as for Pb. This is consistent with the displacement parameters calculated from RMC, shown in the ESI (Table. S6).

Local structure analysis

The experimental pair distribution functions $D(r)$ – defined in the ESI – are shown in Figure 3. The first peak corresponds to the Pb–I nearest neighbour distance at around 3.2 Å, and the position and integrated area are constant for all temperatures on both phases. We note that the tail of the lowest-r PDF peaks overlap with the next higher-r features. The PDFs across the range of distances show little obvious variation with temperature in the cubic phase. The PDFs for the two temperatures in the orthorhombic phase are clearly very different from the PDFs of the cubic phase other than for the first (Pb–I) peak, reflecting the significant differences in crystal structure. For example, the second peak for the cubic phase is a direct overlap of the I–I and Cs–I distances, which have different mean distances in the orthorhombic phase. The PDF for the orthorhombic phase shows more variation between the two temperatures (temperature interval of 180 K) than across the span of temperatures of the cubic phase (100 K), particularly in the distance range 3.5–6 Å where we see the broadening of the peaks on heating.

The distributions of nearest-neighbour distances from the RMC configurations are shown in Figure 4. The interesting point about these diagrams is that the distribution functions are remarkably

asymmetric in each case. For example, the Pb–I distribution has an especially long tail to higher distances, indicating substantial bond anharmonicity; we return to this point in section below. The mean distance at 573 K is 3.27 Å, and a standard deviation on the distribution of $\sigma = 0.25$ Å. The mean distance is around 4% larger than the distances between mean positions (equal to half the lattice parameter, 3.144 Å at 573 K), which is quite common in polyhedral framework materials. The value of σ is consistent with the values of the ADPs; for example, the root-mean-squared displacement of the Pb atom is equal to 0.22 Å from the ADP data. The asymmetry of the I–I and Cs–I distances, which both have mean values around $a/\sqrt{2}$, similarly show a broad asymmetric distribution, reflecting the Pb–I motions.

It is interesting to compare our results here with previous RMC studies of $SrTiO_3$ and $SrSnO_3$.[23,24] In both these cases the distributions of octahedral bond lengths (Ti–O and Sn–O) have much shorter mean values, but also the distributions are narrower and symmetric. Thus the broad, asymmetric distribution of the octahedral bond lengths in $CsPbI_3$ cannot be attributed to the perovskite geometry alone; we return to this point below.

The distribution functions for the linear Pb–I–Pb bond angles, and for perpendicular and linear and I–Pb–I bond, are shown in Figure 5. We show the raw angle distributions $f(\theta)$, where θ is the bond angle, together with the scaled function $f(\theta)/\sin\theta$ to account for the diminishing size of the the solid angle $\mathrm{d}\Omega = \sin\theta \mathrm{d}\theta \mathrm{d}\phi$. The mean angles with standard deviations are $152 \pm 12^\circ$, $89 \pm 15^\circ$, and $157 \pm 11^\circ$ respectively. We can compare the Pb–I–Pb bond angle distributions with the corresponding functions for Ti–O–Ti in $SrTiO_3$[23] and Sn–O–Sn in $SrSnO_3$;[24] other functions were not given in these two publications. The departures from linearity of the Pb–I–Pb bond angle is larger by around 10° than in $SrSnO_3$, whereas at the highest temperature the corresponding angle is just 4° from linearity in $SrTiO_3$.

Rigidity analysis

An alternative to analysing bond angles is to consider the motion of the PbI_6 coordination octahedra as a whole. To analyse the refined RMC configurations in these terms, we used the Geometric

Analysis of Structural Polyhedra (GASP) code.[25–27] GASP is a powerful tool that compares the actual polyhedra within a configuration to ideal polyhedra: here, the refined RMC configuration to the ideal cubic average structure. The sum of the squared distances between corresponding atoms in the two structures, referred to as the "mismatch", is decomposed into components due to rotation of the polyhedra as a rigid unit, bond stretching, and bond bending. Roughly speaking, in the perovskite structure the rotational component corresponds to the low-energy zone-boundary octahedra rotation phonons, while the bond-bending and bond-stretching components correspond to higher-frequency phonons across the Brillouin zone.

Of these three components, we found that bond bending contributed the most to the observed distortion, accounting for 0.52 ± 0.04 of the total mismatch. Rigid-body rotation contributed 0.30 ± 0.04, while bond stretching, expected to be more energetically expensive than bond bending, makes up the remaining 0.18 ± 0.02. Expressed in this way as a percentage of the total mismatch, the values of these three components show negligible temperature dependence between 573 K and 673 K (see ESI), as would be expected.

In Figure 6 we plot the distribution of PbI_6 orientations as determined by the GASP analysis. The mean deviation angle from the average structure at 673 K, with standard deviation, is $8.4 \pm 3.5°$. For comparison, we consider the analogous angles in other perovskite materials. In $SrTiO_3$, which undergoes a displacive phase transition, the TiO_6 octahedra tilt only around 2° in the low temperature phase.[23] On the other hand, in ScF_3, an extremely flexible octahedral framework in which the perovskite A site is vacant, the RMC-derived octahedral tilting angle is around 10° in the high temperature phase.[28]

Anharmonicity

As shown in Fig. 4, the Pb–I bond distribution has an asymmetric shape, a sign of significant anharmonicity. We fitted the distribution data to the Boltzmann form $P(r) \propto \exp(-\phi(r)/k_B T)$,

where $\phi(r)$ is the Morse potential:

$$\phi(r) = \frac{k}{2\alpha^2}\Big(\exp\big(-2\alpha(r-r_0)\big) - 2\exp\big(-\alpha(r-r_0)\big)\Big) \quad (1)$$

The three parameters are r_0, the equilibrium bond length; k, the harmonic spring constant at equilibrium; and α, a measure of the anharmonicity such that the nominal bond dissociation energy is $D = k/2\alpha^2$. We fitted data for all four temperatures together, and obtained reasonable fits to the Pb–I distribution functions between about 2.7 Å and 4.1 Å; above this distance, a slightly greater number of Pb–I pairs are observed than predicted by the Morse potential. The best-fit parameter values are $\alpha = 1.68 \pm 0.04$ Å^{-1}, $r_0 = 3.1559 \pm 0.0007$ Å, and $k = 1.477 \pm 0.003$ meVÅ^{-2}. The value of r_0 is very close to half of the value the cubic lattice parameter values given in Table S1 in the ESI, as expected. The calculated distribution functions are shown in Figure 4 for comparison with the RMC data. The agreement is very good, with the only discrepancy being at larger r which will be in the tail of the Morse function.

Modelling the Pb–I bond as a two atoms joined by a harmonic spring, the vibrational angular frequency is $\omega = \sqrt{k/\mu}$, where $\mu = 78.7\,\mathrm{g\,mol^{-1}}$ is the reduced mass. Substituting in the fitted value of k, we obtain an angular frequency of $\omega/2\pi = 13.2$ THz. The frequency of the longitudinal optic mode at the gamma point is, to first approximation, $\sqrt{2}$ times this value,,[29] namely 18.6 THz; this is comparable, for instance, with literature first-principles calculations that give a value of approximately 17 THz.[13]

Calculating a nominal Pb–I bond dissociation energy from the fitted parameters gives $D =$ 262 meV, which corresponds to an energy considerably in excess of the boiling temperature. This is not a serious discrepancy because we use the α to adjust the anharmonicity near the minimum rather than as a serious indicator of behaviour at large separation.

Given that the fitted values of the Morse potential appear to be plausible, we now consider the implication of the shape of this curve. The function with fitted values is plotted in Figure 7, and compared with the harmonic value calculated from the value of k. It is clear that over the range of

values of distance there is a significant difference that will contribute to the asymmetry of the bond distribution function. At $r = 2.8$ the Morse potential is 1.9 times larger than the harmonic energy relative to the minimum energy, and at $r = 3.8$ the Morse potential is lower than the harmonic value by a factor 2.7. These differences represent the intrinsic anharmonicity of the Pb–I bond, and provides the explanation for the marked asymmetry of the bond distribution function.

Conclusions

In summary, we have performed total neutron scattering measurements, combined with RMC modelling, on the optoelectronically active inorganic perovskite $CsPbI_3$. We report an atomistic model of the cubic α phase showing, in agreement with previous measurements, that there is substantial transverse motion of the I ions. The Pb–I bond is strongly anharmonic, and the distribution of bond distances as a function of temperature is well fitted by a Morse potential with reasonable equilibrium bond length and vibrational frequency. Our real-space picture, in contrast with those that isolate particular vibrational modes, shows that the motion incorporates both zone-center cation off-centering contributions and zone-boundary rigid-body rotations, with the former being somewhat more important. Considering all modes together, we find no evidence for a double-well (bimodal) distribution of atomic positions.

Anharmonicity is a vital consideration for practical use of these materials, since it will substantially affect the structure at useful operating temperatures for photovoltaic devices. It may also be helpful in explaining these materials' behaviour under pressure. This insight into the behaviour of the cubic PbI_6 framework is not only relevant to the inorganic perovskites; it also provides a starting point to understand their hybrid analogues, although in this case the lattice vibrations will be coupled to orientational disorder of the organic cations.[30] Our results emphasise the importance of techniques sensitive to local fluctuations in understanding these materials' true instantaneous structure and consequent behaviour and properties.

Acknowledgement

J.L. is grateful to the China Scholarship Council and Queen Mary University of London for financial support. We also appreciate the beam time from ISIS neutron and muon source. This research utilised Queen Mary's Apocrita HPC facility (http://doi.org/10.5281/zenodo.438045), supported by QMUL Research-IT and funded by EPSRC grants EP/K000128/1 and EP/K000233/1 (M.T.D.).

Supporting Information Available

A single file is available free of charge, which contains the following sections

1. Synthesis
2. Neutron scattering experiments
3. Rietveld refinement
4. Pair distribution functions
5. Reverse Monte Carlo analysis

This material is available free of charge via the Internet at `http://pubs.acs.org/`.

References

(1) Kojima, A.; Teshima, K.; Shirai, Y.; Miyasaka, T. Organometal Halide Perovskites as Visible-Light Sensitizers for Photovoltaic Cells. *Journal of the American Chemical Society* **2009**, *131*, 6050–6051.

(2) National Renewable Energy Laboratory, Best research-cell efficiency chart. 2018; `https://www.nrel.gov/pv/assets/pdfs/best-reserch-cell-efficiencies.pdf`.

(3) Kim, N.-K.; Min, Y. H.; Noh, S.; Cho, E.; Jeong, G.; Joo, M.; Ahn, S.-W.; Lee, J. S.; Kim, S.; Ihm, K.; Ahn, H.; Kang, Y.; Lee, H.-S.; Kim, D. Investigation of Thermally Induced Degradation in $CH_3NH_3PbI_3$ Perovskite Solar Cells using In-situ Synchrotron Radiation Analysis. *Scientific Reports* **2017**, *7*, 838–9.

(4) Eperon, G. E.; Paternò, G. M.; Sutton, R. J.; Zampetti, A.; Haghighirad, A. A.; Cacialli, F.; Snaith, H. J. Inorganic caesium lead iodide perovskite solar cells. *Journal of Materials Chemistry A* **2015**, *3*, 19688–19695.

(5) Saliba, M. Cesium-containing triple cation perovskite solar cells: improved stability, reproducibility and high efficiency. *Energy & Environmental Science* **2016**, *9*, 1989–1997.

(6) Trots, D.; Myagkota, S. High-temperature structural evolution of caesium and rubidium triiodoplumbates. *Journal of Physics and Chemistry of Solids* **2008**, *69*, 2520 – 2526.

(7) Lin, J.; Lai, M.; Dou, L.; Kley, C. S.; Chen, H.; Peng, F.; Sun, J.; Lu, D.; Hawks, S. A.; Xie, C.; Cui, F.; Alivisatos, A. P.; Limmer, D. T.; Yang, P. Thermochromic halide perovskite solar cells. *Nature Materials* **2018**, *17*, 261–267.

(8) Marronnier, A.; Roma, G.; Boyer-Richard, S.; Pedesseau, L.; Jancu, J. M.; Bonnassieux, Y.; Katan, C.; Stoumpos, C. C.; Kanatzidis, M. G.; Even, J. Anharmonicity and Disorder in the Black Phases of Cesium Lead Iodide Used for Stable Inorganic Perovskite Solar Cells. *ACS Nano* **2018**, *12*, 3477–3486.

(9) Hutton, J.; Nelmes, R. J.; Meyer, G. M.; Eiriksson, V. R. High-resolution studies of cubic perovskites by elastic neutron diffraction: $CsPbCl_3$. *Journal of Physics C: Solid State Physics* **1979**, *12*, 5393–5410.

(10) Hutton, J.; Nelmes, R. J. High-resolution studies of cubic perovskites by elastic neutron diffraction. II. $SrTiO_3$, $KMnF_3$, $RbCaF_3$ and $CsPbCl_3$. *Journal of Physics C: Solid State Physics* **1981**, *14*, 1713–1736.

(11) Fujii, Y.; Hoshino, S.; Yamada, Y.; Shirane, G. Neutron-scattering study on phase transitions of $CsPbCl_3$. *Physical Review B* **1974**, *9*, 4549–4559.

(12) Marronnier, A.; Lee, H.; Geffroy, B.; Even, J.; Bonnassieux, Y.; Roma, G. Structural Instabilities Related to Highly Anharmonic Phonons in Halide Perovskites. *Journal of Physical Chemistry Letters* **2017**, *8*, 2659–2665.

(13) Yang, R. X.; Skelton, J. M.; da Silva, E. L.; Frost, J. M.; Walsh, A. Spontaneous Octahedral Tilting in the Cubic Inorganic Cesium Halide Perovskites $CsSnX_3$ and $CsPbX_3$ (X = F, Cl, Br, I). *Journal of Physical Chemistry Letters* **2017**, *8*, 4720–4726.

(14) Ahtee, M.; Kurki-Suonio, K.; VahvaselkÃd', A.; Hewat, A. W.; Harada, J.; Hirotsu, S. Multipole analysis of the nuclear smearing functions in caesium lead trichloride CsPbCl3. *Acta Crystallographica Section B* **1980**, *36*, 1023–1028.

(15) Sakata, M.; Harada, J.; Cooper, M. J.; Rouse, K. D. A neutron diffraction study of anharmonic thermal vibrations in cubic $CsPbX_3$. *Acta Crystallographica Section A* **1980**, *36*, 7–15.

(16) Laurita, G.; Fabini, D. H.; Stoumpos, C. C.; Kanatzidis, M. G.; Seshadri, R. Chemical tuning of dynamic cation off-centering in the cubic phases of hybrid tin and lead halide perovskites. *Chemical Science* **2017**, *8*, 5628–5635.

(17) Tucker, M. G.; Keen, D. A.; Dove, M. T.; Goodwin, A. L.; Hui, Q. RMCProfile: Reverse Monte Carlo for polycrystalline materials. *Journal of Physics: Condensed Matter* **2007**, *19*, 335218.

(18) Stoumpos, C. C.; Malliakas, C. D.; Peters, J. A.; Liu, Z.; Sebastian, M.; Im, J.; Chasapis, T. C.; Wibowo, A. C.; Chung, D. Y.; Freeman, A. J.; Wessels, B. W.; Kanatzidis, M. G. Crystal Growth of the Perovskite Semiconductor CsPbBr3: A New Material for High-Energy Radiation Detection. *Crystal Growth & Design* **2013**, *13*, 2722–2727.

(19) Arnold, O. et al. Mantid—Data analysis and visualization package for neutron scattering and μ SR experiments. *Nuclear Inst. and Methods in Physics Research, A* **2014**, *764*, 156–166.

(20) Larson, A. C.; Dreele, R. B. V. *General Structure Analysis System (GSAS)*; Technical Report 86-748, 1994.

(21) Toby, B. H. EXPGUI, a graphical user interface for GSAS. *Journal of Applied Crystallography* **2001**, *34*, 210–213.

(22) Soper, A. K. *GudrunN and GudrunX: Programs for correcting raw neutron and X-ray diffraction data to differential scattering cross section*; 2011.

(23) Hui, Q.; Tucker, M. G.; Dove, M. T.; Wells, S. A.; Keen, D. A. Total scattering and reverse Monte Carlo study of the 105 K displacive phase transition in strontium titanate. *Journal of Physics: Condensed Matter* **2005**, *17*, S111–S124.

(24) Goodwin, A. L.; Redfern, S. A. T.; Dove, M. T.; Keen, D. A.; Tucker, M. G. Ferroelectric nanoscale domains and the 905 K phase transition in $SrSnO_3$: A neutron total-scattering study. *Physical Review B* **2007**, *76*, 174114.

(25) Wells, S. A.; Dove, M. T.; Tucker, M. G.; Trachenko, K. Real-space rigid-unit-mode analysis of dynamic disorder in quartz, cristobalite and amorphous silica. *Journal of Physics: Condensed Matter* **2002**, *14*, 4645–4657.

(26) Wells, S.; Dove, M.; Tucker, M. Reverse Monte Carlo with geometric analysis - RMC+GA. *Journal of Applied Crystallography* **2004**, *37*, 536–544.

(27) Wells, S. A.; Sartbaeva, A. GASP: Software for geometric simulations of flexibility in polyhedral and molecular framework structures. *Molecular Simulation* **2015**, *41*, 1409–1421.

(28) Dove, M. T.; Du, J.; Keen, D. A.; Tucker, M. G.; Phillips, A. E. A real-space experimental model for negative thermal expansion in scandium trifluoride. `http://arxiv.org/abs/1905.09250`, **2019**.

(29) Dove, M. T. *Structure and dynamics*; Oxford University Press: Oxford, 2002.

(30) Even, J.; Carignano, M.; Katan, C. Molecular disorder and translation/rotation coupling in the plastic crystal phase of hybrid perovskites. *Nanoscale* **2016**, *8*, 6222–6236.

Graphical TOC Entry

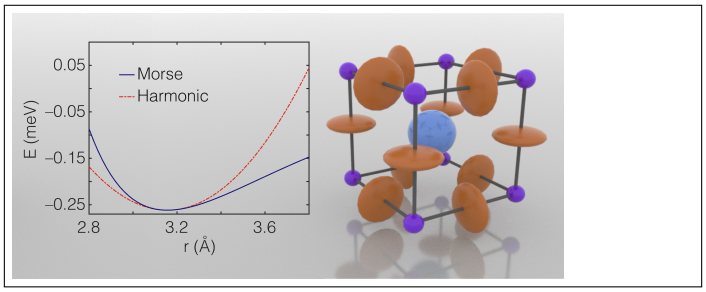

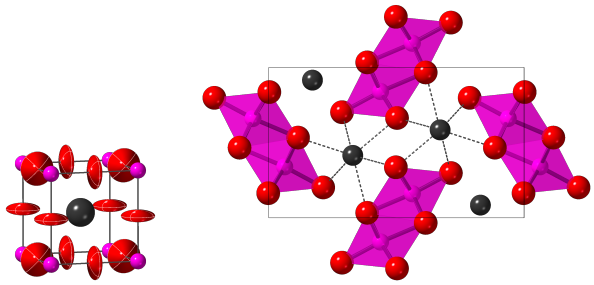

(a) (b)

Figure 1: Refined crystal structure models of (a) cubic α phase at 673 K in three-dimensional perspective, and (b) the orthorhombic δ phase at 293 K viewed down the [010] axis with the [001] axis in the horizontal direction. Cs atoms are grey, Pb atoms are pink. and I atoms are red. In (a) the atoms are represented by ellipsoids to represent their thermal motion, highlighting the large transverse motions of the I atoms. In (b) the PbI_6 coordination is represent by translucent shaded octahedra. We also show the 9 nearest Cs–I neighbours using dashed lines, noting that in this projection three pairs of Cs–I neighbours are directly over one another. Both (a) and (b) are drawn to the same scale.

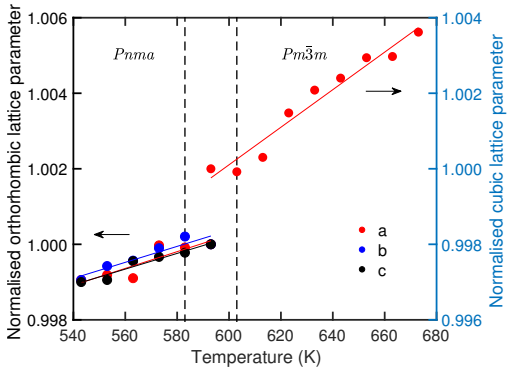

Figure 2: Variation of the lattice parameters of $CsPbI_3$ with temperature, obtained by Rietveld analysis. For convenience, we plot lattice parameters scaled by their values a_0, b_0, c_0 at 593 K. The three lattice parameters of the orthorhombic phase show almost the same thermal expansion. Because of the large change in volume at the phase transition (7% per formula unit), we show the orthorhombic and cubic phases on separate vertical axes; thus the change in volume cannot be read directly from this figure. By contrast, the axes for the orthorhombic (left) and cubic (right) values cover the same difference in relative lattice parameter, so that the thermal expansion of the two phases is directly comparable. Statistical errors of the values of the lattice parameters are smaller than the size of the markers.

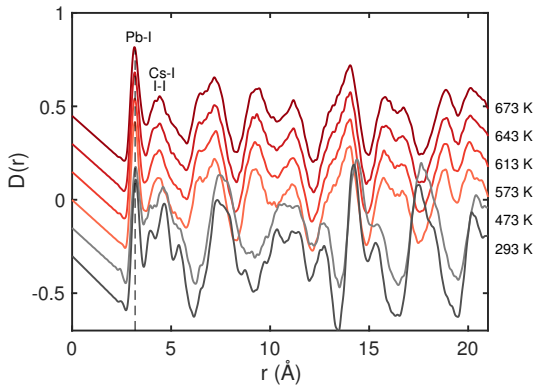

Figure 3: The pair distribution functions $D(r)$ for $CsPbI_3$ for all temperatures where there is a single phase. A constant offset has been applied to separate the separate $D(r)$ curves. The δ phase data are shown in grey and the α phase data in red.

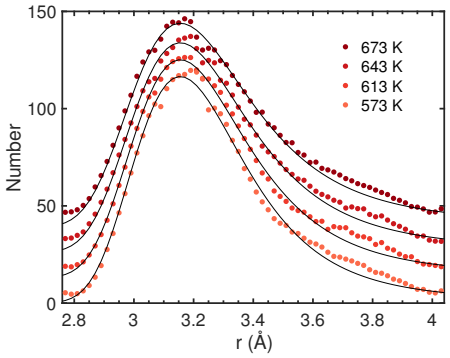

(a) Pb–I

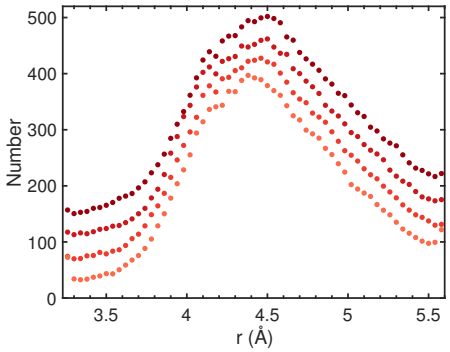

(b) I···I

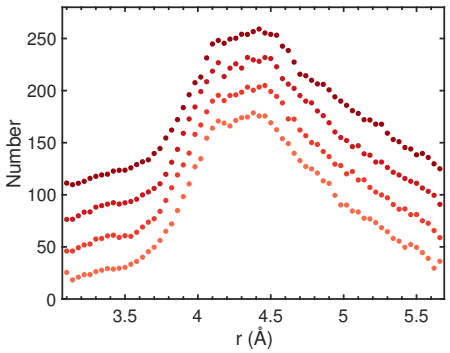

(c) Cs–I

Figure 4: RMC distributions of nearest neighbour distances: (a) Pb–I; (b) I···I; (c) Cs–I. An offset has been added to separate the curves at different temperatures. The continuous curves are the result of fitting to an anharmonic potential energy function as discussed in Section .

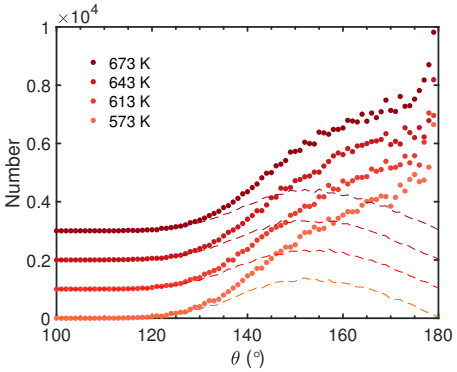

(a) Pb–I–Pb (180°)

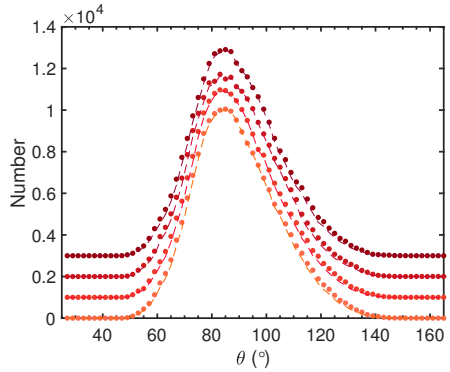

(b) I–Pb–I (90°)

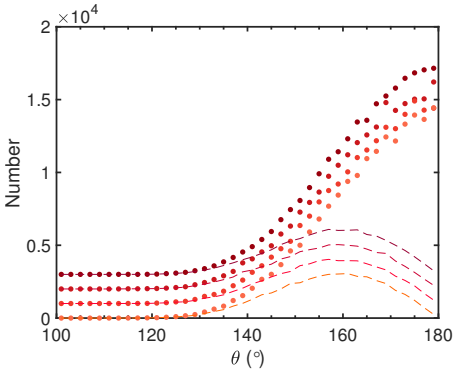

(c) I–Pb–I (180°)

Figure 5: RMC distributions of bond angles θ: (a) Pb–I–Pb (180°); (b) I–Pb–I (90°); (c) I–Pb–I (180°). The pure angle distributions are shown as dashed lines, while the normalised distribution functions by dividing by $\sin\theta$ are plotted with dots. An offset has been added to separate the curves at different temperatures.

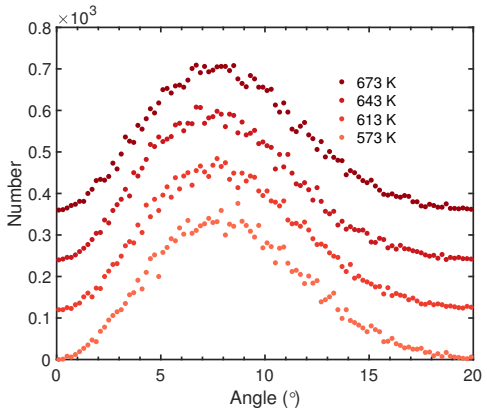

Figure 6: The distribution functions for PbI_6 rotations calculated in the GASP analysis.

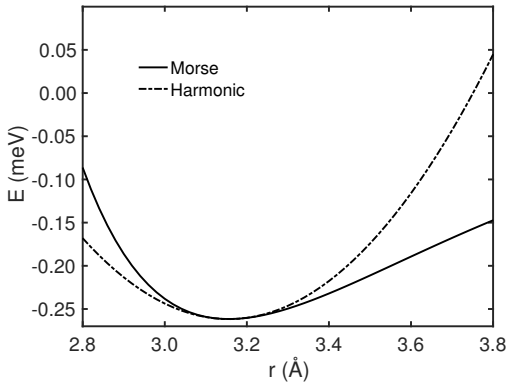

Figure 7: The variation of the Morse potential with distance using the potential parameters given in the text (solid line). This is compared with the corresponding harmonic function (dash-dot line).